DOI: https://doi.org/10.14256/JCE.4503.2026

Građevinar 7/2026

Primljen / Received: 22.1.2026.
Ispravljen / Corrected: 20.5.2026.
Prihvaćen / Accepted: 9.6.2026.
Dostupno online / Available online: 10.8.2026.

Mechanical behavior and damage evolution of high-strength concrete under impact loading

Authors:

Assoc.Prof. **Yu Wu**, PhD. CE
Nanyang Normal University, China
Faculty of Civil Engineering and Architecture
nynuwy@163.com
Corresponding author

Xiaoyang Wu, MCE
Nanyang Normal University, China
Faculty of Civil Engineering and Architecture
wuxiaoyang2536@163.com

Tong Ye, MCE
Nanyang Normal University, China
Faculty of Civil Engineering and Architecture
tongye2026@163.com

Jie Zhou, MCE
Nanyang Normal University, China
Faculty of Civil Engineering and Architecture
nynuzj2018@sina.com

Research Paper

Yu Wu, Xiaoyang Wu, Tong Ye, Jie Zhou

Mechanical behavior and damage evolution of high-strength concrete under impact loading

High-strength concrete (HSC) is widely utilised in impact-resistant and blast-protective structures owing to its superior strength. However, its dynamic mechanical response and cumulative damage evolution under single and repeated impact loading require further clarification, particularly regarding impact pulse duration and strain rate effects. This study investigates the influence of strain rate and striker length on the dynamic mechanical behaviour and damage evolution of C80 HSC. A Ø75 mm split Hopkinson pressure bar system was used to conduct single- and repeated-impact tests at different impact velocities, with 400 mm, 600 mm, and 800 mm strikers. Ultrasonic pulse velocity measurements evaluated damage evolution during repeated impacts, revealing that the fragmentation of the failure modes of C80 HSC intensified with increasing strain rates. The dynamic compressive strength and maximum strain increased with the strain rate, whereas the dynamic elastic modulus remained relatively stable within a certain range. Increasing the striker length prolonged the pulse duration while increasing peak stress and the elastic modulus.

Key words:

high-strength concrete, split hopkinson pressure bar, dynamic mechanical properties, cumulative damage evolution, repeated impact loading

Prethodno priopćenje

Yu Wu, Xiaoyang Wu, Tong Ye, Jie Zhou

Mehaničko ponašanje i razvoj oštećenja betona velike čvrstoće pod udarnim opterećenjem

Beton velike čvrstoće (HSC) široko se primjenjuje u konstrukcijama otpornima na udarna i eksplozivna djelovanja zbog svoje velike čvrstoće. Međutim, njegov dinamički mehanički odziv i razvoj kumulativnog oštećenja pri jednokratnim i višekratnim udarnim opterećenjima još uvijek nisu u cijelosti razjašnjeni, osobito u pogledu trajanja udarnog impulsa i utjecaja brzine deformacije. Ovo istraživanje analizira utjecaj brzine deformacije i duljine udarne šipke na dinamičko mehaničko ponašanje i razvoj oštećenja betona velike čvrstoće razreda C80. Za ispitivanja korišten je sustav Split-Hopkinson tlačne šipke promjera Ø75 mm, pri čemu su provedena ispitivanja pojedinačnog i ponovljenog udara pri različitim brzinama udara, uz primjenu udarne šipke duljine 400 mm, 600 mm i 800 mm. Mjerenjem brzine ultrazvučnog pulsa procijenjen je razvoj oštećenja tijekom ponovljenih udara, pri čemu je utvrđeno da se stupanj fragmentacije pri lomu betona C80 HSC povećava s porastom brzine deformacije. Dinamička tlačna čvrstoća i maksimalna deformacija povećavaju se s porastom brzine deformacije, dok dinamički modul elastičnosti ostaje relativno stabilan u određenom rasponu.

Ključne riječi:

beton velike čvrstoće, Split-Hopkinsonova tlačna šipka, dinamička mehanička svojstva, razvoj kumulativnog oštećenja, višekratno udarno opterećenje

1.Introduction

High-strength concrete (HSC) has advantages such as high strength, good workability, high durability, and low deformability [1-3]. Concrete structures constructed with HSC can replace traditional ordinary concrete, meeting the requirements of modern engineering structures for large spans, heavy loads, and high-rise development, as well as enduring harsh environmental conditions. Additionally, they can reduce component cross sections, increase usable areas, and lower construction costs, yielding significant economic benefits [4, 5]. Recent studies on high-performance cementitious materials have emphasised their importance in improving structural and durability performance. He et al. [6] investigated the coordinated working performance of high-strength reinforcement and ultra-high-performance concrete (UHPC) under cyclic loading, while Zouini et al. [7] evaluated the durability of high-performance concrete reinforced with waste steel fibres. These studies indicate that the mechanical properties and durability of high-performance concrete are important issues in structural engineering applications. Concrete structures are inevitably affected by dynamic loads such as wind loads, earthquakes, and explosions during actual use [8, 9]. Therefore, the impact of dynamic loads on concrete structures must be fully considered during the design and construction processes [10]. As a strain-rate-sensitive material, concrete exhibits different mechanical properties under impact loads than under static loads. Hence, studying the dynamic mechanical properties of HSC under high strain rates is of great significance for seismic design, explosion assessment, and other related fields.

Pioneering dynamic compression tests on concrete were conducted by Abrams [11], who first documented the strain-rate sensitivity of brittle materials such as concrete. Subsequent investigations by both domestic and international scholars have extensively examined the dynamic behaviour of concrete through diverse experimental methodologies, encompassing variations in specimen dimensions and strength grades. Cowell [12] employed cylindrical specimens with compressive strengths of 33.30 and 60.41 MPa for impact testing. The experimental data revealed a significant strain-rate dependence of the compressive strength, with the intrinsic material strength substantially influencing the dynamic strength enhancement. Wakabayashi [13] investigated compressive responses within strain rates ranging from 2×10^{-5} to 1×10^{-1}, establishing a positive correlation between compressive strength and strain-rate elevation. These studies established the fundamental strain-rate-dependent behaviour of concrete, but they mainly focused on single loading conditions and did not fully address the cumulative damage under repeated impact loading.

Concrete behaviour under dynamic loading exhibits significant complexity, governed not only by intrinsic material properties but also by extrinsic factors, including the loading rate, structural geometry, dimensional characteristics, and environmental conditions [14-20]. Abbas [21] investigated the residual mechanical properties of HSC under impact loading using a modified Kolsky compression system incorporating momentum-trapping technology, revealing that stiffness and strength degradation were nearly proportional during the incipient damage stages, whereas stiffness deterioration accelerated beyond strength reduction under progressive damage accumulation. Zhou [22] quantitatively examined the effects of aggregate strength on dynamic tensile performance and damage behaviour through split-tension tests, demonstrating that aggregate strength substantially enhances dynamic tensile properties, and that the aggregate-to-mortar strength ratio critically governs both the failure mechanisms and component-specific damage extent. Subsequently, Guo [15] characterised the mixed-mode fracture damage at rock-concrete interfaces under cyclic shear using acoustic emission (AE) and digital image correlation (DIC), establishing that the petrophysical properties of the rock substrate predominantly dictate the mechanical performance of the specimen. Chen [23] further employed AE monitoring to evaluate the healing efficacy in early-age cementitious systems and determined that damage thresholds were not invariant but exhibited critical dependencies on the curing age and mix proportion parameters. Furthermore, Li [24] conducted synchrotron-based computed tomography (CT) scanning during uniaxial compression and correlated the CT number evolution with damage progression, damage variables, and Poisson's ratio fluctuations, thereby validating these metrics as sensitive indicators for quantifying material degradation severity. These studies demonstrate that damage evolution can be characterised using different monitoring techniques; however, their focus is mainly on the residual properties, tensile damage, interface behaviour, or microscopic damage characterisation, rather than on repeated compressive impact damage in HSC.

The split Hopkinson pressure bar (SHPB) technique serves as an experimental apparatus for investigating damage under dynamic loading. Sun [25] conducted X-ray computed tomography analyses on UHPC and conventional concrete (CC) specimens during dynamic loading, revealing divergent damage evolution mechanisms. UHPC accumulated substantial damage before reaching its peak strength, followed by instantaneous failure upon strength attainment, whereas CC exhibited minimal damage at peak stress, with progressive accumulation exclusively during post-peak softening. Scheiden [26] employed an SHPB integrated with AE monitoring to examine the fatigue damage mechanisms in HSC incorporating granite versus basalt aggregates, demonstrating that granite-aggregate concrete achieved higher fatigue cycles at elevated stress levels, although this trend was reversed at lower stress regimes. Furthermore, Sun [27] identified fundamental disparities in crack propagation between UHPC and CC, establishing that crack parameter measurements correlated with constitutive damage variables confirmed the superior post-peak strain-softening capacity of CC and greater susceptibility of residual mechanical properties (strength/stiffness) to macrocrack development compared with UHPC. Although these SHPB-based studies provide important insights into the dynamic behaviour of cementitious materials, the influence of the striker length and the corresponding stress-wave duration on the repeated-impact response of C80 HSC remains unclear.

Previous studies have extensively examined concrete damage under dynamic loading using diverse experimental methodologies, providing critical references for structural design optimisation. As established in prior studies, significant divergences exist between the dynamic behaviours of HSC and normal-strength concrete (NSC), with research on HSC mechanical characteristics under repeated impacts and varying impact parameters remaining notably scarce. This study is based on the hypothesis that the dynamic mechanical response and cumulative damage evolution of C80 HSC are affected not only by the strain rate but also by the stress-wave characteristics associated with the striker length, especially the pulse duration. To address this knowledge gap, the present study employs a Ø75 mm SHPB system to conduct impact tests on C80 HSC specimens utilising strikers of 400 mm, 600 mm, and 800 mm lengths across multiple velocities. The objectives of this study were to (1) investigate the dynamic mechanical properties of C80 HSC under different impact velocities and striker lengths; (2) clarify the influence of striker length on waveform characteristics, stress-strain responses, and failure modes; (3) evaluate the cumulative damage evolution under repeated impact loading based on ultrasonic pulse velocity measurements; and (4) compare the dynamic performance of C80 HSC with that of C35 NSC.

2. Specimen preparation and experimental design

Based on the literature [28], cubic specimens measuring 150 × 150 × 150 mm were selected for the static tests when the concrete strength exceeded 60 MPa. For impact testing, cylindrical specimens of Ø75 mm × h50 mm were prepared to satisfy the optimal length-to-diameter ratio (L/D = 0.4~1) recommended for SHPB systems [29]. To prevent stress non-uniformity and violation of the stress uniformity assumption due to specimen end-parallelism deviations, the flatness tolerance was strictly maintained within 0.02 mm using precision grinding.

The HSC mix design incorporated high-range water-reducing admixtures and silica fume in addition to cement, coarse aggregates, fine aggregates, and water. Through extensive trial batching in the laboratory, the optimal mix proportions listed in Table 1 were determined to satisfy the requirements of strength, durability, workability, and economic viability. In the C80 mixture, silica fume was used to improve matrix compactness and strength through its filling and pozzolanic effects, whereas a high-range water-reducing admixture was used to maintain adequate workability under a low water-to-binder ratio. Representative cubic and prismatic specimens are illustrated in Figure 1.a, while the dynamically tested specimens are shown in Figure 1b.

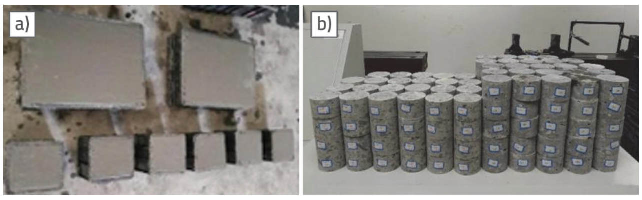

Figure 1. Concrete and sample production (Ø = 75mm, *h* = 50mm): a) Concrete test block; b) Concrete-impact test specimen

2.1. Static testing procedure

To verify compliance with the design strength requirements, the cubic specimens were cured for 3, 7, and 28 days before testing. The specimens were extracted from the curing chamber and subjected to static compression tests using a hydraulic testing machine. Three cubic specimens of each strength grade and curing age were tested. Therefore, 18 cubic specimens were used for the static compressive strength tests of the C35 and C80 concretes. As the impact tests were conducted on the 28-day C80 HSC specimens, Table 2 presents the 28-day static compressive strength results of C80 HSC.

Before testing, the surface moisture of the specimens was removed and the bearing plates of the testing machine were cleaned to ensure proper contact. The specimens were loaded under displacement control at a constant crosshead speed of 0.8-1.0 MPa/s until failure. The peak load was recorded and

Table 1. Concrete mix ratio

Strength grade	Gravel [kg/m³]	Sand [kg/m³]	Cement [kg/m³]	Water [kg/m³]	Silica fume [kg/m³]	Water reducing agent [kg/m³]
C35	1200	620	410	195	0	0
C80	1156	590	540	102	60	24

Table 2. 28-day static compressive strength results of C80 HSC cube specimens

Specimen number	**Load value** [kN]	**Compressive strength** [MPa]
C80-28d-1	1822.88	81.00
C80-28d-2	1871.40	83.20
C80-28d-3	1799.91	80.00
Average value	1831.40	81.40
Standard deviation	36.50	1.64

used to calculate the compressive strength of each specimen (Table 2).

2.2. Impact testing protocol and procedure

To investigate the relationship between the dynamic impact characteristics of C80 HSC and the stress wave parameters (striker length and wave amplitude), tests were conducted using strikers with lengths of 400, 600, and 800 mm. The impact velocities were maintained within the range of 4-10 m/s. As shown in Fig. 2, the SHPB system mainly consists of a high-pressure nitrogen tank, a launch control system, a striker, an incident bar, a transmission bar, an absorbing bar, semiconductor strain gauges, a dynamic strain gauge, and a data acquisition system. During the test, the concrete specimen was placed between the incident bar and the transmission bar, and the two end faces of the specimen were carefully aligned with the bar ends. The standardized procedure for the 600 mm striker is detailed below:

- A 600 mm striker was loaded into the Ø75 mm SHPB system. The strain gauges were calibrated using an empty impact test to determine the calibration factor K for wave signal conversion.
- Before impact, a viscous lubricant (petroleum jelly or grease) was uniformly applied to the specimen surfaces to minimise the interfacial friction. The specimen was then positioned between the incident and transmission bars with precise alignment.
- Impact testing was initiated at low pneumatic pressures, and the chamber pressure was incrementally increased to achieve progressively higher impact velocities. This protocol enables a controlled progression through failure modes, ranging from the intact state to crack initiation, fragmentation, and pulverisation. Impact velocities and waveform data were recorded simultaneously.
- Triplicate tests were performed at each target velocity level, with velocity variations controlled within ±0.2 m/s.

During repeated impact testing, the same specimen was subjected to successive impacts until visible through-cracking, fragmentation, pulverisation, or a complete loss of ultrasonic pulse velocity measurement capability. These conditions were used as the failure criteria to terminate the repeated impact tests.

3. Analysis of single-impact events

3.1. Waveform characteristics

3.1.1. Waveform analysis at varied strain rates

As demonstrated in Figure 3, representative voltage-time waveforms were obtained from C80 HSC cylindrical specimens of Ø75 mm × h50 mm under impact loading using a 600 mm striker bar. For each impact velocity, a representative waveform was selected from the repeated tests. The voltage signals shown in Figure 3 were recorded using semiconductor strain gauges mounted on the incident and transmission bars. The incident and reflected wave signals were obtained from the strain gauge on the incident bar, whereas the transmitted wave signal was obtained from the strain gauge on the transmission bar. The solid lines represent the incident and reflected wave signals, while the dashed lines denote the transmitted wave signals. The incident wave profile of C80 HSC under dynamic

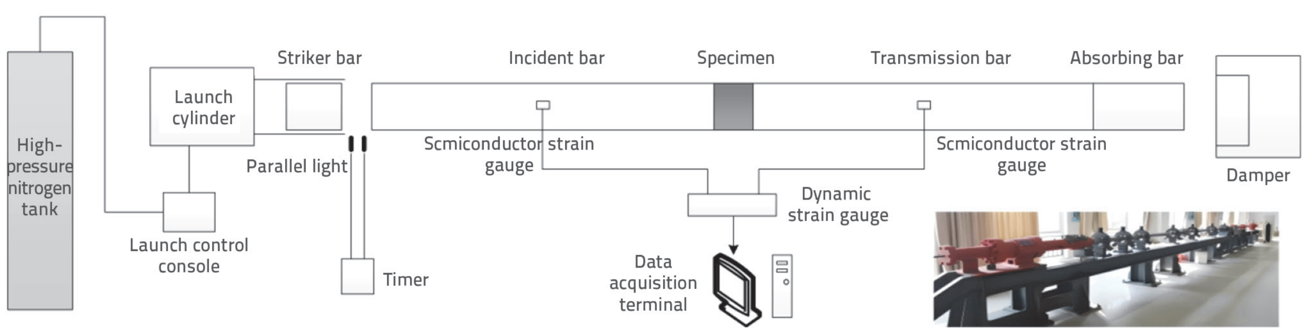

Figure 2. The SHPB impact system used in the experiment

impact manifested as a rectangular pulse. High-frequency oscillations were observed at the wavefront, a phenomenon attributed to dispersion effects during stress wave propagation through the pressure bars. It is evident from the data that higher striker velocities yield higher wave amplitudes. According to the one-dimensional elastic wave theory,

$$\sigma = \frac{\rho_0 c_0 v}{2} \quad (1)$$

where ρ_0 and c_0 denote the density and elastic wave velocity of the pressure bar, respectively, a linear relationship between incident wave amplitude and impact velocity is established. This theoretical prediction is generally consistent with experimental observations.

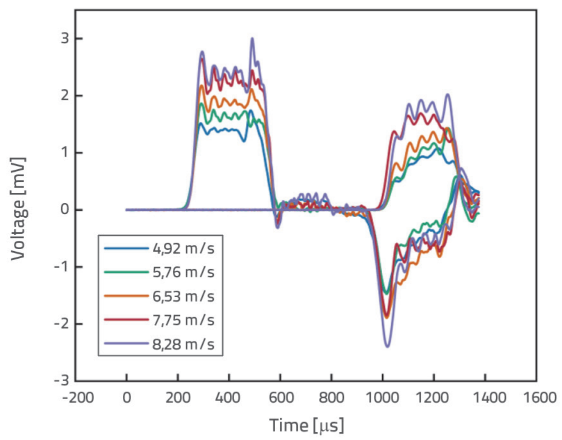

Figure 3. Voltage-time waveforms of C80 HSC using a 600 mm long striker

As the impact velocity increased, the propagation paths and reflection cycles of the stress waves within the concrete specimens were altered by the newly generated microcracks and voids. The amplitude of the reflected waves is governed by the superposition effects from multiple reflections, with magnitude variations serving as indicators of damage morphology. This mechanism accounted for the irregular shapes of the reflected waveforms. At elevated velocities, waveform profiles exhibit two characteristic phenomena:

- Reflected waves develop a distinct "W"-shaped profile, where the definition of this profile correlates positively with the severity of damage progression.
- Transmitted waves demonstrate linear decay patterns, signifying through-thickness crack propagation and rapid stress release upon reaching the ultimate strength limit.

As evidenced by post-test examinations, the "W"-shaped reflection coupled with linear transmission decay emerges exclusively when C80 HSC specimens undergo fragmentation. This waveform signature constitutes a distinctive manifestation of brittle failure mechanisms in HSC. This characteristic contrasts markedly with the failure behaviour observed in NSC.

3.1.2. Waveform analysis at varied striker lengths

To evaluate striker length effects on waveform characteristics, representative voltage-time waveforms of C80 HSC cylindrical specimens of Ø75 mm × h50 mm were analysed using striker lengths of 400 mm, 600 mm, and 800 mm. To reduce the influence of impact velocity, representative tests with comparable impact velocities and incident wave amplitudes were selected for comparison. Voltage signals were obtained using the measurement method described in Section 3.1.1. The superimposed waveform comparisons are presented in Figure 4.

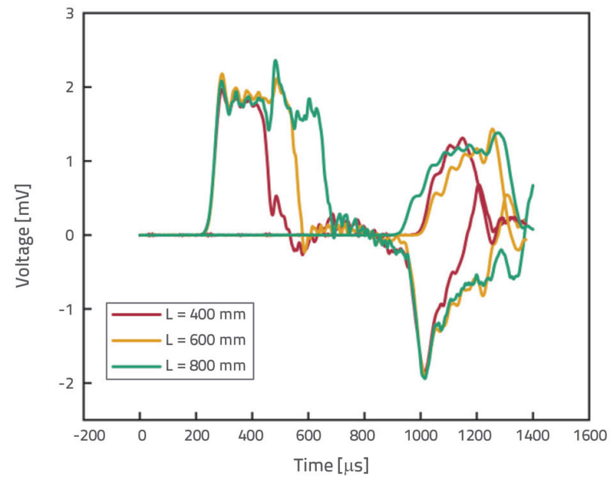

Figure 4. Voltage-time waveform of C80 HSC specimens under three different striker lengths

The solid lines represent the incident and reflected wave signals, whereas the dashed lines denote the transmitted wave signals. Based on Figure 4, the following analyses are presented:

- A distinct correlation between the pulse duration (i.e., the loading time) of the incident waves and the striker length was demonstrated, wherein longer strikers yielded increased pulse durations, irrespective of the impact velocity. According to the elastic wave propagation theory:

$$T = \frac{2L}{c_0} \quad (2)$$

  where T represents the pulse duration, L denotes the striker length, and c_0 is the constant elastic wave velocity in the steel pressure bars (5060 m/s). This equation establishes that the pulse duration proportionally increases with the striker length, which agrees with the observed waveform tendency.
- Under comparable impact velocities (4-10 m/s), the incident wave amplitudes do not exhibit a clear monotonic dependence on the striker length. This suggests that the striker length mainly affects the pulse duration, whereas its influence on the incident wave amplitude is relatively limited.

3.2. Analysis of dynamic stress-strain curves for HSC

The dynamic stress-strain behaviour of C80 HSC cylindrical specimens with Ø75 mm × h50 mm, as shown in Figure 1(b), under a 600 mm striker impact is characterised in Figure 5a. The strains and stresses were calculated from the incident, reflected, and transmitted strain signals recorded by semiconductor strain gauges mounted on the incident and transmission bars. After calibration and voltage-to-strain conversion, the specimen stress, strain rate, and strain were obtained based on the one-dimensional stress wave theory of SHPB testing as follows:

$$\sigma_s(t) = \frac{E_b A_b}{A_s}\varepsilon_t(t) \tag{3}$$

$$\dot{\varepsilon}_s(t) = -\frac{2C_b}{L_s}\varepsilon_r(t) \tag{4}$$

$$\dot{\varepsilon}_s(t) = -\frac{2C_b}{L_s}\int_0^t \varepsilon_r(t)\,dt \tag{5}$$

Where $\sigma_s(t)$, $\tilde{\varepsilon}_s(t)$ and $\varepsilon_s(t)$ are the stress, strain rate, and strain of the specimen, respectively; E_b, A_b, and C_b are the elastic modulus, cross-sectional area, and elastic wave velocity of the pressure bars, respectively; A_s and L_s are the cross-sectional area and length of the specimen, respectively; and $\varepsilon_r(t)$ and $\varepsilon_t(t)$ are the reflected and transmitted strain signals, respectively. At identical striker lengths, the following mechanical responses are observed:

- Elastic phase: The stress increases linearly with minimal strain accumulation, indicating a high dynamic elastic modulus.
- Post-peak phase: Upon reaching the first peak stress, plastic deformation dominates, as manifested by a limited stress elevation and rapid strain development.

The strain-rate dependence is demonstrated through two distinct regimes:

- Low strain rates: Near-linear stress-strain relationships were maintained during the intermediate stages, corresponding to the undamaged specimens.
- Elevated strain rates: Curvilinear profiles emerge, with the curve morphology governed by the impact velocity and progressive damage evolution. The distinctive curve variations reflect the differential failure patterns.

Figure 5b presents stress-strain curves obtained from C80 HSC specimens impacted by strikers of varying lengths (400 mm, 600 mm, 800 mm) within a comparable strain rate range (66-69 s^{-1}). The key observations are as follows:

- Elastic phase characteristics: Increased striker lengths tended to produce higher peak stresses, whereas the dynamic elastic modulus showed significant scatter among the specimens.
- 400 mm striker: Limited loading duration generally resulted in reduced peak stress and peak strain, while the elastic modulus showed some scatter. The constitutive behaviour exhibited distinct elastoplastic characteristics.
- 800 mm striker: The prolonged loading duration generally produced higher stress and strain responses, accompanied by more pronounced deformation characteristics in the constitutive curve.
- 600 mm striker: A less pronounced deformation phase was observed relative to the 800 mm case, with the deformation modulus values varying among specimens rather than presenting a strictly consistent trend.

3.3. Deformation and failure analysis

The experimentally determined dynamic mechanical properties of C80 concrete subjected to striker impacts at lengths of 400, 600, and 800 mm are summarised in Table 3. Considering that the heterogeneity of concrete and the sensitivity of the SHPB result in local damage initiation, the strain rate and dynamic elastic modulus exhibit a certain degree of scatter. Therefore, the following discussion focuses on the overall trends. The number is denoted by "DM" followed by a number, where "DM" refers to the specimens used for dynamic mechanical parameter tests. The dynamic elastic modulus was determined by linear fitting of the initial, approximately linear portion of the dynamic stress-strain curve.

Experimental data analysis revealed a proportional relationship between impact velocity and strain rate elevation. The failure modes were categorised as intact, through-cracking, fragmentation, and pulverisation, and the morphological evolution is illustrated in Figure 6.

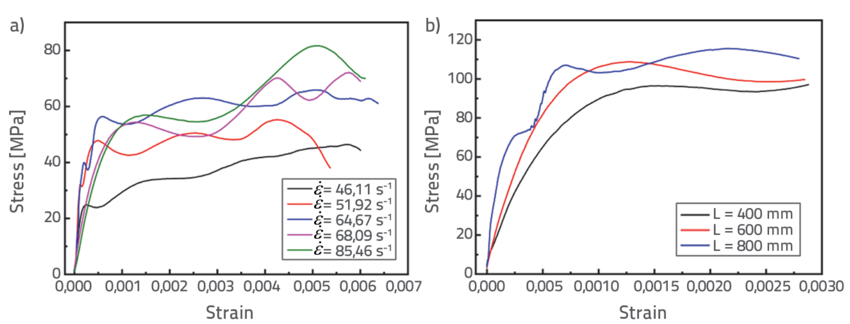

Figure 5. Dynamic stress-strain curves of C80 HSC specimens with Ø75 mm × h50 mm: a) Under different strain rates with a 600 mm striker; b) Stress-strain curves under impact bars (L) of different lengths

Table 3. Dynamic mechanical parameters of C80 concrete

Number	Striker length [mm]	Impact speed [m/s]	Strain rate [s⁻¹]	Peak strength [MPa]	Maximum strain [×10 ⁻⁶]	Dynamic elastic modulus [GPa]	Failure mode
DM-1	400	4.83	52.19	45.25	6228.44	129.42	Intact
DM-2		6.15	66.66	58.48	6552.94	175.94	Through-cracking
DM-3		7.91	83.48	71.81	7971.06	153.39	Fragmentation
DM-4		8.82	86.88	74.84	10 668.95	128.02	Fragmentation
DM-5		9.59	93.57	88.39	9809.87	261.92	Pulverisation
DM-6	600	4.88	55.13	49.88	8352.87	219.03	Intact
DM-7		5.70	50.68	55.74	7142.92	358.53	Intact
DM-8		5.76	52.67	64.35	6100.10	176.62	Intact
DM-9		6.49	64.95	67.68	7955.74	257.96	Through-cracking
DM-10		6.53	67.48	67.48	9224.47	179.97	Through-cracking
DM-11		7.55	74.67	73.67	10 876.76	196.75	Fragmentation
DM-12		7.75	66.06	75.51	8767.66	257.98	Fragmentation
DM-13		8.28	85.46	90.13	10 353.58	269.156	Pulverisation
DM-14	800	5.36	52.70	60.37	9478.28	154.6	Intact
DM-15		5.83	56.67	63.68	7514.46	166.53	Intact
DM-16		6.28	69.49	67.41	12 577.19	111.20	Fragmentation
DM-17		7.08	66.94	77.23	10 001.80	135.89	Fragmentation
DM-18		8.12	78.09	86.49	10 808.97	273.60	Pulverisation
DM-19		8.28	62.50	92.22	7193.22	282.00	Pulverisation

Intact (Low Velocity): Minimal incident wave amplitudes induce internal microdamage without visible surface manifestations (Figure 6.a). The specimens retained their structural integrity despite the initiation of the subsurface damage.
Through-cracking (Moderate Velocity): Increased wave amplitudes drive rapid development of through-thickness cracks. Crack arrest occurred without specimen disintegration, preserving the macrostructural continuity (Figure 6.b).
Fragmentation (High Velocity): Critical wave amplitudes trigger shear-dominated failure at the aggregate-mortar interfaces, resulting in multi-fragment separation (Figure 6.c).
Pulverisation (Ultrahigh velocity): Catastrophic disintegration manifests as explosive fragment ejection. Petrographic analysis confirmed the predominance of aggregate fractures in this failure regime (Figure 6.d).

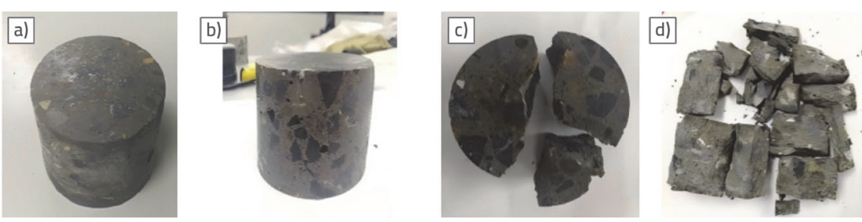

Figure 6. Failure form of HSC C80: a) Intact; b) Penetrating crack; c) Fragmented into pieces; d) Crushed

4. Damage analysis under impact loading

4.1. Definition and measurement of damage variable

The damage variable serves as a quantitative metric for assessing the degradation of the structural integrity and mechanical performance of concrete. Current methodologies define concrete damage variables through cross-sectional area reduction or degradation of the elastic modulus.Due to measurement uncertainties associated with these physical parameters, the damage variable D is formulated based on the elastodynamic theory as follows:

$$D = 1 - \left(\frac{\bar{v}_p}{v_p} \right)^2 \quad (6)$$

Where $\bar{v}_p$ and v_p represent the post-impact and initial ultrasonic pulse velocities, respectively.

Experimental Procedure: Instrumentation: An RSM-SY5 ultrasonic tester with longitudinal wave transducers was utilised.for specimen Alignment: Specimens were coaxially aligned between transducers. Coupling: A thin grease layer was applied at specimen-transducer interfaces, with uniform contact pressure maintained at 0.05 ± 0.01 MPa (per ASTM D6087-08). Measurement Protocol: Ultrasonic wave velocities were recorded before and after impact. The damage variables were subsequently computed using equation (6).

4.2. Damage under single impact

For single-impact tests on the HSC specimens, impact experiments were conducted using strikers of varying lengths at distinct velocities. Ultrasonic pulse velocity measurements were performed before and after each impact to quantify damage evolution through longitudinal wave velocity assessments. The resulting damage variables, calculated according to the methodology outlined in Section 4.1, are systematically listed in Table 4. The number is denoted by "DA" followed by a number, where "DA" refers to the specimens used for ultrasonic damage assessment. The impact of a 600 mm striker is considered here as an example.

Analysis of the tabulated data reveals that single-impact damage exhibits inherent dispersion for each striker length, while still showing an overall increasing tendency with increasing impact speed. Within the detectable damage threshold, the damage magnitude remains minimal at lower impact velocities and increases progressively with higher impact velocities. As evidenced by the experimental results, impact-induced damage correlated strongly with velocities exceeding 5.5 m/s, indicating that the energy required for crack propagation was sufficiently supplied at this critical threshold, thereby facilitating stable fracture development. Conversely, lower-energy impacts produce damage with stochastic characteristics, although they are consistently maintained at quantitatively reduced levels. The damage values in Table 4 show an overall increasing tendency with increasing impact speed, but the increase is not strictly monotonic for all specimens. This scatter is primarily attributed to the inherent heterogeneity of concrete, local differences in aggregate distribution and microcrack initiation, and possible variations in ultrasonic coupling after impact. Therefore, the single-impact damage results were interpreted in terms of the overall tendency rather than strictly consistent point-by-point growth.

To elucidate the correlation between damage evolution and striker length, three discrete velocity levels-4.00 m/s, 5.20 m/s, and 6.00 m/s-were selected for systematic analysis. The quantified damage-length relationships are presented in Table 5.

Damage evolution is intrinsically governed by the striker length and impact velocity. Key experimental findings include:(1) Constant striker length: At 400 mm length,

Table 4 Damage values under single impact (600 mm)

Number	Impact speed [m/s]	Longitudinal wave velocity before damage [m/s]	Longitudinal wave velocity after damage [m/s]	Damage value. D
DA-1	3.45	3846	3125	0.072
DA-2	4.17	4545	3125	0.312
DA-3	4.18	3846	2778	0.278
DA-4	4.25	4545	3125	0.312
DA-5	4.51	3846	2941	0.235
DA-6	4.77	3846	3333	0.133
DA-7	4.87	3846	3125	0.187
DA-8	4.9	3846	2941	0.235
DA-9	4.97	3846	3125	0.187
DA-10	5.09	3846	2632	0.316
DA-11	5.10	3333	2778	0.167
DA-12	5.20	4545	3846	0.154
DA-13	5.50	3846	2632	0.216
DA-14	5.79	3846	3571	0.187
DA-15	5.81	3846	3333	0.198
DA-16	5.85	3846	2941	0.235
DA-17	6.18	3846	3333	0.323
DA-18	6.21	3846	2273	0.409
DA-19	6.57	4167	3571	0.543

Table 5 Damage Values of HSC with different striker lengths

Striker length [mm]	**Impact speed** [m/s]	**Damage value**
400	4.00	0.083
	5.20	0.133
	6.00	0.154
600	4.00	0.278
	5.20	0.316
	6.00	0.409

damage variable D increased by 0.071 when velocity escalated from 4.00 to 6.00 m/s, whereas a ΔD of 0.131 was recorded for 600 mm strikers. The damage accumulation exhibited a positive velocity dependence. (2) Constant impact velocity: Damage initiation occurred at lower threshold velocities with increasing striker length. Specifically, the minimum impact velocity required to induce damage in C80 concrete decreased proportionally with the striker length, accelerating the damage progression rates. (3) Differential growth kinetics: At a striker length of 400 mm, the damage developed gradually with increasing velocity. Conversely, steeper damage velocity gradients were observed for longer strikers (600/800 mm). (4) Length-damage correlation: Under equivalent velocities (e.g. 5.20 m/s), the striker length is positively correlated with the damage increment magnitude (Table 5).

4.3. Damage evolution under repeated impact

4.3.1. Repeated impact testing protocol

Concrete structures in service are frequently subjected to repetitive dynamic loads (e.g., blast-induced stress waves and seismic excitations), leading to fatigue-induced damage accumulation from irreversible microstructural alterations. Beyond the single-impact analysis, this section investigates the damage evolution in C80 HSC under repeated impact loading.

In contrast to single-impact tests, repeated impact investigations require identical incident wave amplitudes to evaluate the mechanical properties and damage evolution of C80 HSC under cyclic loading, which prioritises determining the impact velocities specific to each striker length, ensuring that C80 specimens withstand at least five repeated impacts. The standardized procedure for 400 mm strikers is detailed below:

Impact velocity calibration: Initial impacts were performed at low velocities, followed by incremental increases of 0.2 m/s until satisfying three criteria: a) Ultrasonic wave velocity remains measurable; b) No visible cracking occurs post-impact; c) Specimens endure ≥ 5 consecutive impacts. Repeated impact execution. For striker lengths of 400 mm and 600 mm, impacts were administered at constant velocities (±0.5% variation). The 800 mm striker was excluded from the repeated-impact tests because preliminary tests showed that it produced excessive damage during the early impact stages. Testing continued until crack propagation or pulverisation occurred, and three specimens with the same dimensions and mix proportions were tested for each velocity-striker length combination.

Damage monitoring: Ultrasonic pulse velocity measurements were performed after each impact cycle.

4.3.2. Waveform analysis under repeated impact

The waveform profiles of the C80 HSC specimens subjected to repeated impacts at consistent incident wave amplitudes are presented in Figure 7, where the solid lines represent the incident and reflected wave signals, whereas the dashed lines denote the transmitted wave signals.

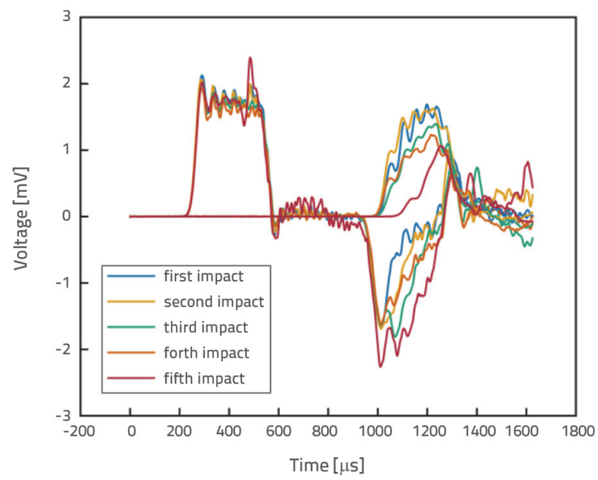

Figure 7. The test piece repeats the impact at a length of 600 mm striker

Critical observations from the reflected and transmitted waves include the following. For the reflected waves, the initial reflection peak occurs earlier than the subsequent peaks (Impacts 2-3 times), with temporal convergence observed in later impacts (Impacts 3-4 times). For the transmitted waves, peak emergence was delayed during the first impact compared with subsequent events.

According to the three-wave analysis equations governing SHPB systems, instantaneous stress-strain states are uniquely determined by the incident, reflected, and transmitted wave amplitudes. Progressive waveform evolution manifests as the reflected wave amplitudes increasing monotonically with the impact number, accompanied by progressive temporal retardation of the peak occurrence. The transmitted wave amplitudes decrease systematically, whereas the peak emergence exhibits a progressive temporal advancement.

This phenomenon is attributed to microvoid proliferation within the concrete under cumulative damage. The phase reversal between the initial and subsequent reflected waves induces peak retardation, whereas a consistent phase orientation in the transmitted waves accelerates peak emergence. Notably, under equivalent incident amplitudes, longer strikers accelerated both the rate of reflected wave attenuation and transmitted wave augmentation during repeated impacts.

4.3.3. Stress-strain curve under repeated impact action

The stress-strain curves for repeated impacts with two different striker lengths are shown in Figures 8.

Analysis of the stress-strain curves revealed that their variation trends were consistent with the waveform diagrams. The peak stress of the concrete specimen during the first impact was greater than those during the second and third impacts, whereas the peak stresses during the second and third impacts were essentially identical. The slope during the third impact showed a significant increase compared with the fourth and fifth impacts, indicating that the internal pores of the HSC closed after the third impact, whereas new cracks were generated during the fourth impact, leading to increased damage to the concrete specimen. Consequently, the peak stress and deformation modulus during the fourth impact are significantly lower than those during the third impact. The curve generated by the fourth impact exhibits a decrease in the elastic phase and an increase in the plastic phase. With a striker length of 400 mm, the elastic phase during the final impact was small but still discernible, whereas with a striker length of 600 mm, the elastic phase during the final impact was almost non-existent, transitioning directly into the plastic phase. This is a result of cumulative damage with increasing impact time.Under continuous repeated impacts, the maximum strain corresponding to the failure of the concrete specimens increased gradually with an increase in the number of impacts. This is due to the accumulation of damage caused by repeated impacts on the concrete, leading to a gradual increase in strain. Repeated impacts on the concrete specimens increased the internal pores and cracks, resulting in a decrease in the measured longitudinal wave velocity and a gradual increase in damage.

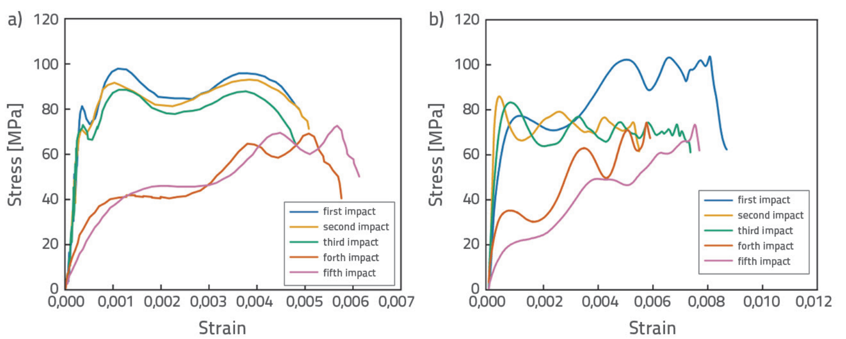

Figure 8. Stress-strain curve: a) Repeated impact with 400 mm striker length; b) Repeated impact with 600 mm striker length

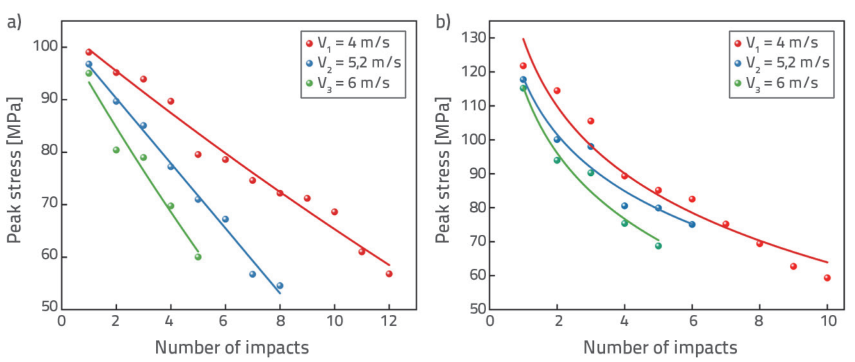

Figure 9. Relationship between peak stress and number of impacts: a) Repeated impact of 400 mm striker length; b) Repeated impact of 600 mm striker length

4.4. Relationship between impact parameters and impact frequency

The mechanical parameters of the concrete specimens subjected to repeated impacts from two different striker lengths are listed in Table 6. The repeated impact results shown in Table 6 were obtained at a nominally calibrated impact velocity of approximately 4 m/s. The listed impact speeds are the measured values for each impact and exhibit slight fluctuations around the nominal value. Therefore, the analysis focuses on the overall cumulative damage evolution and the influence of striker length. When the post-impact ultrasonic pulse velocity was recorded as 0 m/s, it indicates that no stable ultrasonic signal could be detected because of severe cracking or fragmentation; the corresponding cumulative damage was therefore taken as D = 1.

The relationship between the number of impacts and the peak strength when

Table 6. Dynamic characteristics of C80 HSC subjected to cyclic impact

Striker length [mm]	Number of impacts	Impact speed [m/s]	Amplitude [MPa]	Peak stress [MPa]	Maximum strain (×10 $^{-6}$)	Longitudinal wave velocity before damage [m/s]	Longitudinal wave velocity after damage [m/s]	Cumulative damage value
400	1	4.04	80.36	99.03	2879.32	3846	3333	0.133385
	2	3.74	74.39	95.15	3238.99	3333	3125	0.195792
	3	3.82	75.9	93.92	3549.45	3125	2941	0.254672
	4	3.88	77.17	89.70	3625.03	2941	2778	0.310095
	5	4.06	80.75	79.57	3670.03	2778	2632	0.362651
	6	3.73	74.19	78.60	3771.95	2632	2548	0.394566
	7	3.81	75.78	74.62	3882.64	2548	2381	0.460107
	8	4.22	83.94	72.17	3904.09	2381	2174	0.547045
	9	3.92	77.97	71.21	3970.91	2174	1923	0.662501
	10	4.31	85.73	68.62	4260.36	1923	1615	0.822667
	11	4.21	83.74	61.00	4404.78	1615	1515	0.884587
	12	3.97	78.96	56.80	4561.81	1515	0	1
600	1	4.24	84.33	121.78	3863.26	4145	3333	0.195899
	2	3.89	77.37	104.47	4300.50	3333	3125	0.258305
	3	4.02	79.96	86.52	4459.43	3125	2947	0.315265
	4	4.20	83.54	84.36	4623.64	2947	2732	0.38822
	5	4.26	84.73	83.15	4875.19	2732	2581	0.443491
	6	3.72	73.99	82.54	5395.76	2581	2374	0.523693
	7	4.25	84.53	78.19	5422.44	2374	1927	0.711983
	8	4.08	81.15	74.42	5477.46	1927	1623	0.869741
	9	4.17	82.94	72.72	5736.43	1623	1515	0.936284
	10	4.02	79.96	68.34	5784.67	1515	0	1

repeatedly impacting concrete specimens at different striker lengths and velocities is shown in Figures 9. For the same striker length, the peak strength decreased as the number of impacts increased, indicating greater internal damage to the concrete specimens. When the striker length was 400 mm and the velocity was approximately 4 m/s, the specimen could withstand 12 impacts. The peak strength of the specimen decreased slightly during the first four impacts but decreased significantly after the fourth impact. This phenomenon was due to the closure of internal pores in the concrete during early impacts, followed by the initiation of new cracks during subsequent impacts, which caused gradual fragmentation. When the concrete specimens are repeatedly impacted at velocities v_1 = 4.0 m/s, v_2 = 5.2 m/s, and v_3 = 6 m/s, it was observed that as the impact velocity increased, the number of impacts gradually decreased, and the peak strength decreased faster; furthermore, the longer the striker length, the fewer the impacts. This phenomenon indicated that as the number of impacts increased, the internal damage of the specimens gradually accumulated. The first impact compressed the internal pores of the specimen, causing significant damage, whereas the second and third impacts continued to increase the internal cracks in the specimen, albeit at a reduced damage growth rate. Under repeated impacts, the cracks gradually

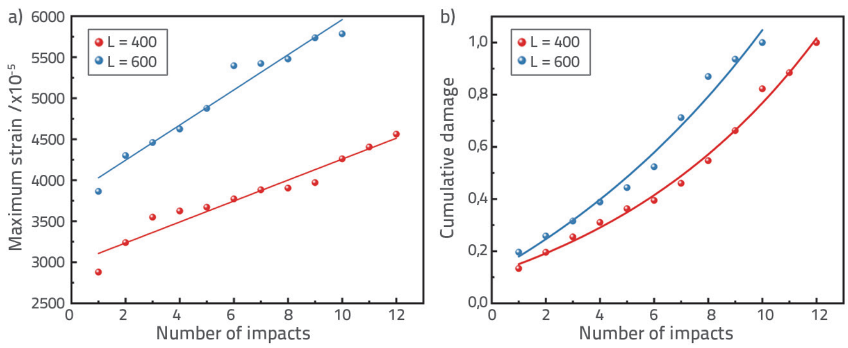

Figure 10 The relationship between maximum strain, cumulative damage, and impact frequency: a) Relationship between impact times and maximum strain, b) Relationship between impact times and maximum strain

increased, and damage accumulated continuously until the specimen fragmented during the final impact. The fitting curve relating the number of impacts and peak strength was approximately linear when the striker length was 400 mm, whereas it exhibited a concave profile when the striker length was 600 mm, indicating that the striker length caused the peak stress to decrease at different rates. As shown in Figure 9, the peak strength decreases rapidly during the first few impacts but decreases more slowly during later impacts, with higher impact velocities accelerating this peak strength degradation.

The impact time should be more than eight to better reflect the entire process of HSC under repeated impacts. Therefore, this paper selects velocities near 4.0 m/s as examples to create a relationship diagram between the impact times and maximum strain. As shown in the figure, the strain and number of impacts are positively correlated, with the strain continuously increasing as the number of impacts increases. According to the "three-wave" formula, strain is calculated based on the information of reflected waves, and the variation pattern of strain reflects the evolution of damage. For the same striker length, the strain gradually increased with an increase in impact time. When the concrete was repeatedly impacted at the same velocity, the strain generated during the last impact was much larger than that generated during the first impact, indicating progressive internal damage accumulation. As the number of impacts increased, the resistance of the strong concrete specimens to impact decreased, which was reflected in the reduction in the peak strength. This is consistent with the pattern of impact times and peak strengths observed in the previous section. The deformation was reflected as a gradual increase in the maximum strain. As shown in Figure 10.a, at the same velocity, the impact time gradually decreases as the striker length increases, whereas the maximum strain increases.

Figure 10.b illustrates the relationship between the impact frequency and cumulative damage in HSC. From Figure 9.b, it can be observed that for the same striker length, the cumulative damage gradually increased with an increase in the impact frequency. The cumulative damage increases slowly during the first four impacts but increases rapidly after the fourth impact, exhibiting a trend of slow increase followed by a rapid increase, which is more pronounced when the striker length is 400 mm. When the striker length was 600 mm, there was no obvious trend of a slow increase followed by a rapid increase, and the number of times the cumulative damage increased slowly was shorter than that observed for the 400 mm striker. This is also consistent with the previously introduced behavioural trends; hence, further elaboration is omitted here. Furthermore, for different striker lengths, the longer the striker length, the faster the cumulative damage increased with an increase in the impact frequency.

5. Comparison of dynamic mechanical properties between C35 concrete and C80 HSC

To investigate the differences in mechanical properties between HSC and ordinary concrete under impact, impact tests were conducted on two types of specimens with the same size but different strength grades at a strain rate of approximately 50 s^{-1}, and the differences in their dynamic performance were compared. To provide a clearer comparison, the main dynamic mechanical responses of C35 concrete and C80 HSC at comparable strain rate ranges are summarised in Table 7.

As shown in Figure 11.a, the dynamic elastic modulus of the C80 HSC was significantly higher than that of the C35 concrete, and the first peak point of the C80 concrete was also higher than that of the C35 concrete. During the elastic phase, both types of concrete exhibit a linear increase in strain with a slight increase in stress. After reaching the first peak point, the C80 concrete produced new cracks, indicating that the elastic deformation had reached its limit stage, and the subsequent behaviour was mainly characterised by plasticity development. However, there was a significant difference between the C35 and C80 concretes after reaching the first peak point. The stress-strain curve of the C35 concrete exhibits a plateau phase, during which the stress remains essentially unchanged as the strain increases, exhibiting a strain-softening phenomenon, followed

Table 7. Dynamic Response Comparison between C35 Concrete and C80 HSC

Concrete class / Parameter	C35	C80	Comparison
Peak stress	Lower	Higher	C80 shows higher dynamic resistance
Dynamic elastic modulus	Lower and more scattered	Higher overall	C80 exhibits higher stiffness
Maximum strain	Larger	Smaller	C35 shows greater deformation
Strain-rate effect	Increases with strain rate	Increases with strain rate	Both show strain-rate sensitivity
Post-peak behavior	More obvious softening	More abrupt stress drop	Failure behaviour differs
Possible damage mechanism	Pore closure and interface damage	Denser matrix and aggregate-related fracture	Further microscopic evidence is needed

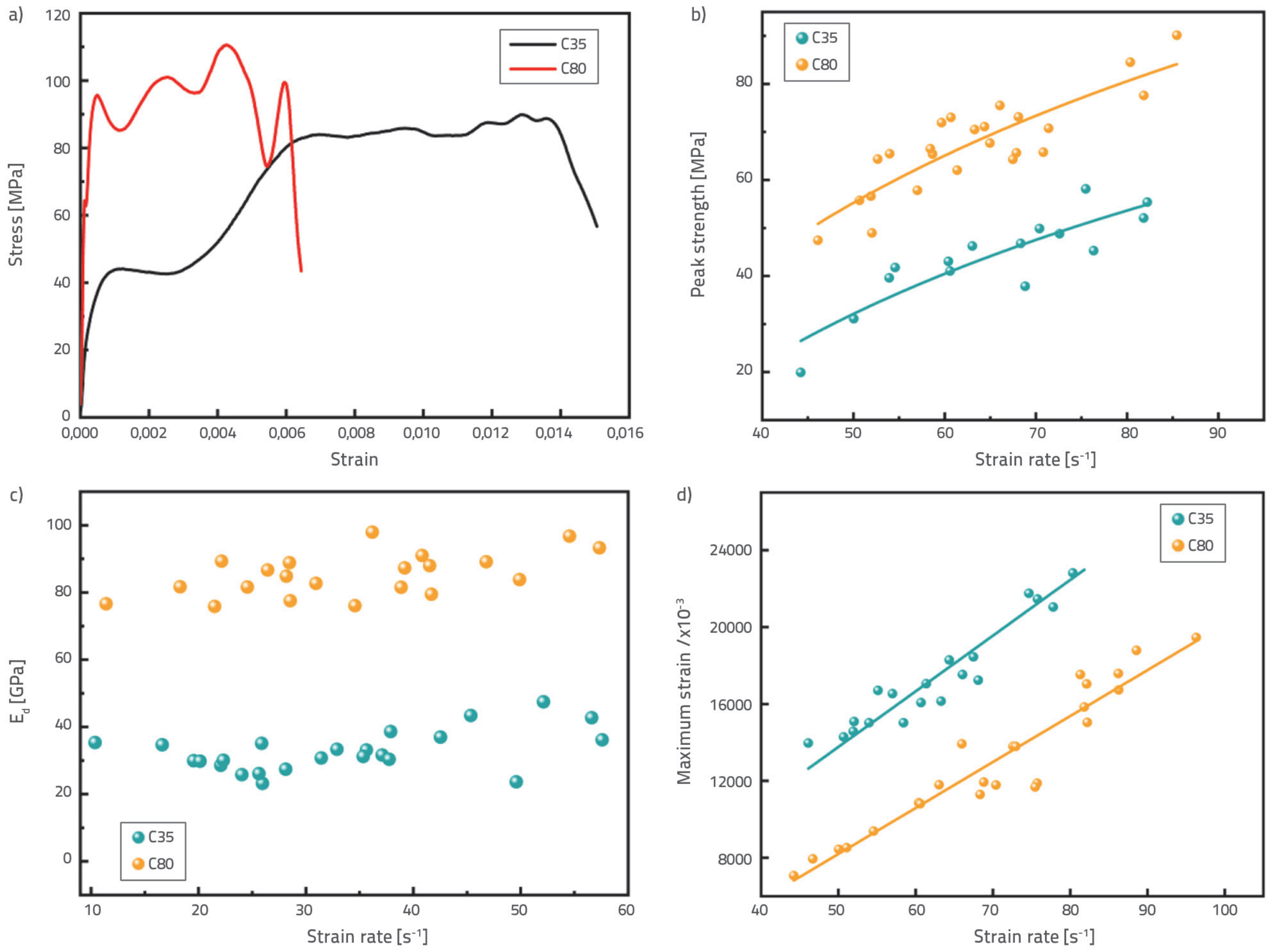

Figure 11 Dynamic mechanical properties between C35 concrete and C80: a) Dynamic stress-strain curves; b) Peak stress-strain rate relationship; c) Dynamic elastic modulus-strain rate relationship; (d) Maximum strain-strain rate relationship

by a gradual increase in stress. This is because of the presence of a large number of pores in the C35 concrete, which close when subjected to an external load impact. In contrast, the C80 HSC is internally denser, thus eliminating the strain-softening phenomenon. During the unloading phase, the C80 concrete exhibited a linear downward trend, whereas the C35 concrete exhibited a gentler downward trend. This is attributed to the different failure mechanisms of the two types of concrete: C80 HSC mainly experiences the failure of coarse aggregates, whereas C35 concrete experiences the failure of the binding between coarse aggregates and cementitious materials.

The peak stress-strain rate curves for the two strength grades of concrete, fitted based on the experimental data, are shown in Figure 11.b. Under the same strain rate conditions, the peak stress of the C80 HSC was approximately 1.5 times that of the C35 concrete, which is more clearly demonstrated by the data in the figure, that HSC has a higher dynamic compressive strength. The strength increases of C35 and C80 HSC at a strain rate of 82 s^{-1} relative to 60 s^{-1} are 14.67 MPa and 26.76 MPa, respectively, indicating that the strength increase of concrete increases with the increase of strength grade. Figure 11b shows that the peak stress of the concrete specimens with two different strengths increased with strain rate, exhibiting a significant strain rate effect. The slopes of the fitted peak stress-strain rate curves for the two strength concretes were nearly identical, indicating that concretes with different strength grades had similar increases.

As shown in Figure 11.c, the dynamic elastic modulus of concrete with two different strengths changed within a certain range as the strain rate increased. However, the trend of the change was negligible, indicating that the dynamic elastic modulus of concrete was not rate-sensitive. However, there are differences in opinions among scholars, both domestically and internationally. The conclusion of this study is consistent with that of Zhao et al. [31]; however, Wang et al. [32] concluded that the dynamic elastic modulus increases with an increase in the strain rate, while Su et al. [33] reported that it decreases with an increase in the strain rate. This may arise under the continuous impact load, the degree of microcrack propagation, and the strength of different parts within different concrete specimens can affect the dynamic elastic modulus. Testing methods under different conditions can also affect the elastic modulus, which may be one of the reasons why scholars hold different views on the dynamic elastic modulus. As shown in Figure 11c, the dynamic elastic modulus of specimen C80 was significantly higher than that of specimen C35. This conclusion is directly related to the strength grade of the concrete. Compared with C80 HSC, C35 concrete may contain more internal pores and a less compact matrix. Under impact loading, possible pore closure and interfacial damage may lead to larger deformation and a lower apparent dynamic elastic modulus. However, as the strength increases, the internal compactness of the concrete increases, the amount of aggregate also increases, the water-cement ratio becomes relatively small, and there are fewer internal pores. Therefore, the elastic modulus of the HSC is larger.

From Figure 11d, it can be observed that (1) the maximum strain of the concrete specimens with different strength grades increases with increasing strain rate. This phenomenon is due to the crack-induced deformation of concrete when subjected to an external load. However, owing to the short loading time, the internal bearing capacity of the concrete remained intact, resulting in a larger peak strain in the concrete specimens. (2) Under the same strain rate, the maximum strain of the C35 concrete was approximately 1.5 times that of the C80 concrete, indicating that the C35 concrete exhibited more pronounced deformation under the same strain rate. When the strain rate increased from 50 s^{-1} to 80 s^{-1}, the maximum strain of C35 increased by 0.01046, whereas that of C80 HSC increased by 0.00807. From Figure 11d, it can be observed that the slope of the maximum strain-strain rate curve for C35 is greater than that for C80, indicating that HSC not only has a lower maximum strain but also exhibits a lower rate sensitivity. This phenomenon may be related to the denser internal structure of C80 HSC and its lower deformation capacity under dynamic loading. Owing to the presence of more internal pores, ordinary concrete experiences greater deformation when subjected to impact, whereas HSC, with its denser internal structure, experiences less deformation. Therefore, under dynamic impact conditions with the same conditions, HSC exhibits a lower sensitivity to changes in the maximum strain rate.

6. Conclusion

To analyse the mechanical properties of HSC under impact, impact tests were conducted on C80 HSC specimens using different striker lengths and velocities through the SHPB test system, obtaining the dynamic impact performance of HSC. The longitudinal-wave velocities of the specimens were measured using ultrasonic waves for damage detection and failure analysis. The impact performances of ordinary concrete were compared and studied. The main conclusions are as follows:

- Under single-impact loading, the incident wave amplitude increased with the impact velocity, whereas the pulse width was mainly related to the striker length. With an increasing strain rate, the peak stress and maximum strain of the C80 HSC generally increased, while the striker length mainly affected the pulse duration and damage development rate. At comparable strain rates, longer strikers tended to produce higher stress responses because of the longer loading duration. However, the peak stress was primarily governed by the strain rate and incident wave amplitude rather than by the striker length alone. At the same striker length, the damage evolution rate increased with the impact velocity, and longer strikers promoted faster damage development.
- Under repeated impact loading, the maximum strain increases with the number of impacts, whereas the peak strength gradually decreases. Internal cracks and cumulative damage develop progressively during repeated impacts. For the same striker length, a higher impact velocity reduced the number of impacts required for failure and accelerated the decrease in peak strength. Under the same impact velocity, the specimens impacted by longer strikers failed after fewer impacts and showed a larger maximum strain, indicating that a longer pulse duration accelerated the cumulative damage.
- Under the same striker length and impact velocity, the waveforms of the C35 and C80 concrete were similar when the incident wave amplitudes were similar. After damage occurred at higher impact velocities, the reflected wave of the C35 concrete exhibited a U-shaped profile, whereas that of the C80 HSC exhibited a W-shaped profile. The first peak stress and dynamic elastic modulus of the C80 HSC were significantly higher than those of the C35 concrete. The C35 concrete exhibited more obvious strain softening after the first peak, whereas the C80 HSC exhibited a higher dynamic stiffness and lower maximum strain sensitivity. These differences are related to the denser internal structure of the HSC and the different damage mechanisms of the two types of concrete.

Acknowledgements

The authors gratefully acknowledge financial support from Henan Provincial Science and Technology Research Projects (Grant Nos. 252102320207, 252102321016, 262102320347) and Nanyang Normal University Doctoral Special Project (Grant Nos. 2020ZX007, 2026QN019). Thanks are given to members of the Structural Impact Laboratory for assistance in SHPB system operation and experimental data processing.

REFERENCES

[1] Shin, H.O., Yoo, D.Y., Lee, J.H., Lee, S.H., Yoon, Y.S.: Optimized mix design for 180 MPa ultra-high-strength concrete, Journal of Materials Research and Technology, 8 (2019) 5, pp. 4182–4197.

[2] Kumar, R., Singh, S., Singh, L.P.: Studies on enhanced thermally stable high strength concrete incorporating silica nanoparticles, Construction and Building Materials, 153 (2017), pp. 506–513.

[3] Bedon, C., Amadio, C.: Enhancement of the seismic performance of multi-storey buildings by means of dissipative glazing curtain walls, Engineering Structures, 152 (2017), pp. 320–334.

[4] Gangolu, J., Kumar, A., Bhuyan, K., Sharma, H.: Probabilistic demand models and performance-based fragility estimates for concrete protective structures subjected to missile impact, Reliability Engineering & System Safety, 223 (2022), Article 108497.

[5] Mechtcherine, V.: Novel cement-based composites for the strengthening and repair of concrete structures, Construction and Building Materials, 41 (2013), pp. 365–373.

[6] He, S., Tian, L., Li, M.: Experimental investigation of the coordinated working performance of high-strength reinforcement and UHPC under varying parameters, GRAĐEVINAR, 78 (2026) 2, pp. 95-105, https://doi.org/10.14256/JCE.4360.2025

[7] Zouini, R., Amjad, U., Irshidat, M., Makani, A.: Durability assessment of high-performance concrete reinforced with waste steel fibres, GRAĐEVINAR, 77 (2025) 12, pp. 1225-1232, https://doi.org/10.14256/JCE.4295.2025

[8] Hao, H., Bi, K., Chen, W., Pham, T.M., Li, J.: Towards next generation design of sustainable, durable, multi-hazard resistant, resilient, and smart civil engineering structures, Engineering Structures, 277 (2023), Article 115477.

[9] Maluk, C., Bisby, L., Terrasi, G.P.: Effects of polypropylene fibre type and dose on the propensity for heat-induced concrete spalling, Engineering Structures, 141 (2017), pp. 584–595.

[10] Asprone, D., Jalayer, F., Prota, A., Manfredi, G.: Proposal of a probabilistic model for multi-hazard risk assessment of structures in seismic zones subjected to blast for the limit state of collapse, Structural Safety, 32 (2010) 1, pp. 25–34.

[11] Abrams, D.A.: Effect of rate of application of load on the compressive strength of concrete, 1917.

[12] Cowell, W.L.: Dynamic Properties of Plain Portland Cement Concrete, 1966.

[13] Wakabayashi, M., et al.: Dynamic loading effects on the structural performance of concrete and steel materials and beams, Proceedings of the 7th World Conference on Earthquake Engineering, Vol. 6, Turkish National Committee on Earthquake Engineering, 1980.

[14] Jin, L., Kaixin, L., Zhang, R., Yu, W., Du, X., Deng, X.: Combined effects of cryogenic temperature and strain rates on compressive behavior of concrete, International Journal of Damage Mechanics, 31 (2022).

[15] Guo, Y.B., Gao, G.F., Jing, L., Shim, V.P.W.: Dynamic Properties of Mortar in High-strength Concrete, International Journal of Impact Engineering, 165 (2022), Article 104216.

[16] Williams, B., Heard, W., Graham, S., Nie, X.: Effect of specimen geometry on triaxial compressive response of high-strength concrete, Construction and Building Materials, 244 (2020), Article 118348.

[17] Khaliq, W., Mujeeb, A.: Effect of processed pozzolans on residual mechanical properties and macrostructure of high-strength concrete at elevated temperatures, Structural Concrete, 20 (2019), pp. 307–317.

[18] Guo, Y.B., Gao, G.F., Jing, L., Shim, V.P.W.: Response of high-strength concrete to dynamic compressive loading, International Journal of Impact Engineering, 108 (2017), pp. 114–135.

[19] Zhou, W., Tang, L., Liu, X., Ma, G., Chen, M.: Mesoscopic simulation of the dynamic tensile behaviour of concrete based on a rate-dependent cohesive model, International Journal of Impact Engineering, 95 (2016), pp. 165–175.

[20] del Viso, J.R., Carmona, J.R., Ruiz, G.: Shape and size effects on the compressive strength of high-strength concrete, Cement and Concrete Research, 38 (2008) 3, pp. 386–395.

[21] Abbas, M.A., Williams, B.A., Heard, W.F., Nie, X.: Residual mechanical properties of high strength concrete BBR9 subjected to dynamic uniaxial compressive loading, Cement and Concrete Research, 180 (2024), Article 107488.

[22] Zhou, X., et al.: Meso-scale numerical simulation of the effect of aggregate strength on damage and fracture of high-strength concrete under dynamic tensile loading, Theoretical and Applied Fracture Mechanics, 122 (2022), Article 103551.

[23] Guo, Y., Chen, X., Wang, Z., Ning, Y., Bai, L.: Identification of mixed mode damage types on rock-concrete interface under cyclic loading, International Journal of Fatigue, 166 (2023).

[24] Li, N., Zhao, Y., Xing, Y., He, X., Li, H.: Meso-damage analysis of concrete based on X-ray CT in-situ compression and using deep learning method, Case Studies in Construction Materials, 18 (2023), Article e02118.

[25] Sun, Q., Martin, B., Williams, B., Heard, W., Frew, D., Nie, X.: Comparative study on the impact-induced microstructural damage in concrete using X-ray computed micro-tomography, Mechanics of Materials, 168 (2022), Article 104277.

[26] Timmermann, T., Oneschkow, N.: Influence of coarse aggregate type on the damage mechanism in high-strength concrete under compressive fatigue loading, Structural Concrete, 20 (2019), pp. 1212–1219.

[27] Sun, Q., Martin, B., Williams, B., Heard, W., Frew, D., Nie, X.: Comparative study on the impact-induced microstructural damage in concrete using X-ray computed micro-tomography, Mechanics of Materials, 168 (2022).

[28] Sun, Q., et al.: Comparative study of strength-based damage evolution in ultra-high-performance concrete (UHPC) and conventional concrete (CC) under dynamic loading, International Journal of Impact Engineering, 155 (2021).

[29] Liu, Z., Jiang, L., Cheng, G., Yan, C., Li, Z.: Size effect on compressive and tensile strength of high-strength concrete, Science Technology and Engineering, 15 (2015) 30, pp. 209–213.

[30] Li, S., Liu, D., Li, X., Kang, H., Wang, L.: Experimental study on length effect of φ75 mm split Hopkinson pressure bar specimens, Journal of China University of Mining & Technology, (2010) 1.

[31] Zhao, P., Lok, T., Lu, G.: Using the Split Hopkinson-Bar to investigate dynamic behavior of SFRC, Magazine of Concrete Research, 55 (2003), pp. 183–191.

[32] Wang, S., Zhang, M.-H., Quek, S.T.: Mechanical behavior of fiber-reinforced high-strength concrete subjected to high strain-rate compressive loading, Construction and Building Materials, 31 (2012), pp. 1–11.

[33] Su, H., Xu, J.: Dynamic compressive behavior of ceramic fiber reinforced concrete under impact load, Construction and Building Materials, 45 (2013), pp. 306–313.